

# Real-Time 141 GHz JCAS Channel Sounder: Near-Field Switched Beamforming, Carrier Multiplexing, and Context Awareness

Jihoon Bang<sup>1</sup>, Samuel Berweger<sup>1</sup>, Jack Chuang<sup>1</sup>, Camillo Gentile<sup>1</sup>, *Member, IEEE*,  
Nada Golmie<sup>2</sup>, *Fellow, IEEE*, and Sebastian Semper<sup>3</sup>

**Abstract**—We have developed a real-time 141 GHz joint communications and sensing (JCAS) channel sounder, with focus on this article on 3-D near-field imaging (less than 50 cm range) for applications such as finger recognition. To achieve this, we integrated phased-array antennas into the channel sounder—to the best of our knowledge, we are the first to do so in the D-band—and adapted the switched beamforming technique we developed previously, to realize real-time near-field beamforming. We also propose another novel technique, coined *carrier multiplexing*, to extend the instantaneous bandwidth of the phased arrays to their full radio frequency (RF) passband—by a factor of two for our current arrays and by a factor of ten for our next edition. Finally, we integrated camera and Lidar systems that are temporally and spatially synchronized with the channel sounder to generate real-time digital twins of the target while sounding, enabling machine learning on multimodal data. We showcase system performance with controlled experiments on metal cylinders, demonstrating imaging resolution on the order of a centimeter.

**Index Terms**—Calibration, channel measurement, channel modeling, D-band, propagation, 6G, sub-terahertz, sub-THz, 3-D imaging.

## I. INTRODUCTION

THE evolution of wireless networks over the last 40 years has witnessed ever wider bandwidths, ever more antennas, and ever shorter packet durations, all for the sole purpose of delivering higher communications throughput. As a byproduct, today's networks have fine enough resolution in the respective delay (range), angle (space), and Doppler-frequency shift (velocity) domains to enable sensing the contours of

relatively small targets by way of Radar [1]. Unlike optical sensors, Radar is insensitive to lighting conditions and colors, can operate in nonline-of-sight conditions, maintains privacy and has low enough power consumption for a device to operate for years on a single battery [2]. What is more, the pervasiveness of today's networks—composed of small cells, relays, Wi-Fi routers, and other access points in addition to cell towers—enables ubiquitous sensing for Internet of Things (IoTs) applications such as target classification (e.g., human, vehicle, and UAV) [3], human pose reconstruction [2], [4], [5], human activity recognition (e.g., walking, jumping, and sitting), [6], [7], [8] and hand and finger recognition (e.g., swiping, rolling, and signing) [9], [10], [11], [12], [13], [14], [15], [16], [17], [18], [19], [20], [21], [22]. The extension of network functionality from communications alone to sensing has paved the way for joint communications and sensing (JCAS) as the defining trait of 6G networks.

The Terahertz regime is attractive for JCAS applications thanks to tens of Gigahertz of available bandwidth and to sub-millimeter wavelengths for packing hundreds of antennas in close proximity (nominally half-wavelength apart). The sub-Terahertz D-band—110–170 GHz—is particularly attractive due to lesser oxygen-absorption pathloss [23], prompting the debut of D-band channel sounders in recent years, which we catalog in the next paragraph. A comprehensive literature on Terahertz channel sounders (beyond just the D-band) can be found in [24] and [25] and is beyond the scope of this article.

Vector network analyzer (VNA)-based sounders, which sweep the frequency domain across the band of interest, are the most common [26], [27], [28], [29], [30], [31], [32], [33], [34], [35], [36], [37], [38]; but because they sweep such a wide band, can take up to 45 s [28]. With free-space pathloss at sub-Terahertz even greater than at millimeter-wave [23], pencilbeam directional antennas will be employed to compensate the link budget by virtue of high gain; but to obtain omnidirectional field-of-view (FoV), the most typical setup is to sweep the angle domain by placing the antennas on mechanical rotators: VNA-based variants perform 2-D (azimuth only) [30], [31], [32] or 3-D (azimuth and elevation) [33] angle sweeps at the receiver (RX) only (single directional), 2-D angle sweeps at the transmitter (TX) and RX (double directional) [27], [34], and 3-D double-directional

Received 23 December 2024; revised 7 January 2025; accepted 9 January 2025. Date of publication 28 January 2025; date of current version 9 June 2025. (*Corresponding author: Camillo Gentile.*)

Jihoon Bang is with the Communications Technology Laboratory, National Institute of Standards and Technology, Boulder, CO 80305 USA, and also with the Department of Physics, University of Colorado, Boulder, CO 80305 USA (e-mail: jihoon.bang@nist.gov).

Samuel Berweger is with the Communications Technology Laboratory, National Institute of Standards and Technology, Boulder, CO 80305 USA (e-mail: samuel.berweger@nist.gov).

Jack Chuang, Camillo Gentile, and Nada Golmie are with the Communications Technology Laboratory, National Institute of Standards and Technology, Gaithersburg, MD 20879 USA (e-mail: jack.chuang@nist.gov; camillo.gentile@nist.gov; nada.golmie@nist.gov).

Sebastian Semper is with the Institute for Information Technology, Technische Universität Ilmenau, 98693 Ilmenau, Germany (e-mail: sebastian.semper@tu-ilmenau.de).

Digital Object Identifier 10.1109/TMTT.2025.3529345

U.S. Government work not protected by U.S. copyright.

angle sweeps [35], [36]; the slow mechanical movement, however, extends the total sweep duration—across both frequency and angle—from tens of seconds to minutes or even hours. The alternative to rotators are virtual phased-array antennas, which are traced out by placing the antennas on 2-D [37] or 3-D [38] positioners and then beamformed in postprocessing to sweep angle, but due to mechanical translation are as slow. The alternative to VNAs are correlation-based sounders [23], [39], [40], [41], [42], [43] that transmit a pseudorandom-noise (PN) code and then correlate at the RX—effectively sweeping delay instead of frequency—reducing the sweep duration from tens of seconds to just nanoseconds; but when coupled with 2-D [41] or 3-D rotators [23], [42], [43] to sweep double-directional angle, their speed advantage vanishes vis-à-vis the mechanical movement.

The slow sweep duration of the aforementioned channel sounders is much beyond the tens or hundreds of microseconds coherence time desired for D-band channels [25]. It is not by chance that they have been thus far employed to characterize environments only, as environments can be maintained static during the sweep; the sole exception is [29], which characterizes the Radar-cross section (RCS) of a human that is maintained static during the sweep. Notwithstanding, these channel sounders are beneficial to the current work underway by the 3rd Generation Partnership Project (3GPP) to extend the frequency range (currently valid up to 100 GHz) of their popular 38.901 channel propagation model [45] that characterizes environments—urban, rural, office, and factory classes—for 5G communications applications. Besides frequency range, another important extension is the classes of models characterized, from environments classes only to target classes—e.g., human, vehicle, and UAV classes—for 6G sensing applications.

In the 38.901 model, an environment is represented as a collection of discrete multipath components, each representing a planar wavefront that scatters radiated power randomly in the delay, angle, and Doppler domains. While sufficient to evaluate communications performance metrics such as throughput, how a target scatters power in these domains in a temporally consistent manner—e.g., applications for hand recognition—is the very radio frequency (RF) signature that characterizes a target, so real-time channel sounding is necessary. Since the RF signature of a target will be characterized by the motion of its individual parts—e.g., the independent motion of human hands—high resolution in these domains to discriminate the parts is paramount.

However, the much greater propagation pathloss in the D-band, where the finest angle and delay resolution for sensing are available, will limit applications from centimeters to tens of meters [4], [5], [6], [7], [8], [9], [10], [11], [12], [13], [14], [15], [16], [17], [18], [19], [20], [21], [22] rather than to hundreds or thousands of meters that are typical for communications [46]. At these distances, near-field beamforming—which assumes that the wavefronts are spherical, not planar as in the far-field, so the beam pattern varies not only with angle, but also with delay—is subscribed. Hence, the angle rotation of fixed-beam directional antennas is inadequate [23], [27], [30], [31], [32], [33], [34], [35],

[36], [41], [42], [43]; and although virtual phased-array antennas [37], [38] are capable of near-field beamforming, they cannot operate in real-time.

In this article, we describe a novel 141 GHz JCAS channel sounder, with the following main contributions.

- 1) *Real-Time*: To the best of our knowledge, we are the first to develop a D-band channel sounder with real (not virtual) phased-array antennas, so that angle can be swept electronically (not mechanically), enabling a total channel sweep in just 512  $\mu$ s.
- 2) *Carrier Multiplexing*: To achieve high-resolution imaging, we developed a technique to extend the instantaneous bandwidth of our current arrays by multiplexing adjacent RF bands, each linked to a separate carrier frequency. This technique required extending our previous work on generating the TX waveform in a single band [47], [48] to partitioning the waveform across multiple bands.
- 3) *Near-Field Switched Beamforming*: We adapted the switched beamforming technique that we developed previously for estimating angle-of-departure (AoD) at the TX and angle-of-arrival (AoA) at the RX of communications channels in the far-field [47], to near-field imaging. This adaptation introduced significant advancements, addressing the unique challenges of near-field operation, such as focusing beams at finite ranges and accounting for the curvature of spherical wavefronts.
- 4) *Context Awareness*: We complemented the RF system of the channel sounder with a spatially and temporally synchronized camera/Lidar system, to generate a real-time digital twin of the target during sounding, for training machine learning algorithms on multimodal data [22], as well as many other applications [49], [50].

Naturally, since the far-field is an approximation of the near-field, the channel sounder can also be deployed at longer distances to characterize communication channels (in addition to Radar imaging). Consistent with our previous communications channel sounders [47], [51], [52], [53], we can also deembed the properties of the channel sounder—such as the TX waveform, antenna patterns, and hardware nonidealities—ensuring that the channel data produced is generalizable. Specifically, it can generalize to any TX waveform with bandwidth less than the channel sounder's and to any antenna pattern with beamwidth greater than the channel sounder's [54], [55], [56]. The channel sounder can thereby support a wide range of JCAS applications.

The remainder of this article is structured as so: Section II describes the channel sounder architecture, namely the RF system and the camera and Lidar systems. Section III describes the carrier multiplexing technique that we developed followed in Section IV by our near-field switched beamforming technique. Section V showcases controlled experiments on metal cylinders with dimensions comparable to human fingers, and Section VI summarizes our current and future work.

## II. CHANNEL SOUNDER ARCHITECTURE

The architecture of the channel sounder is described in this section. First, we describe the RF system—the phased-array

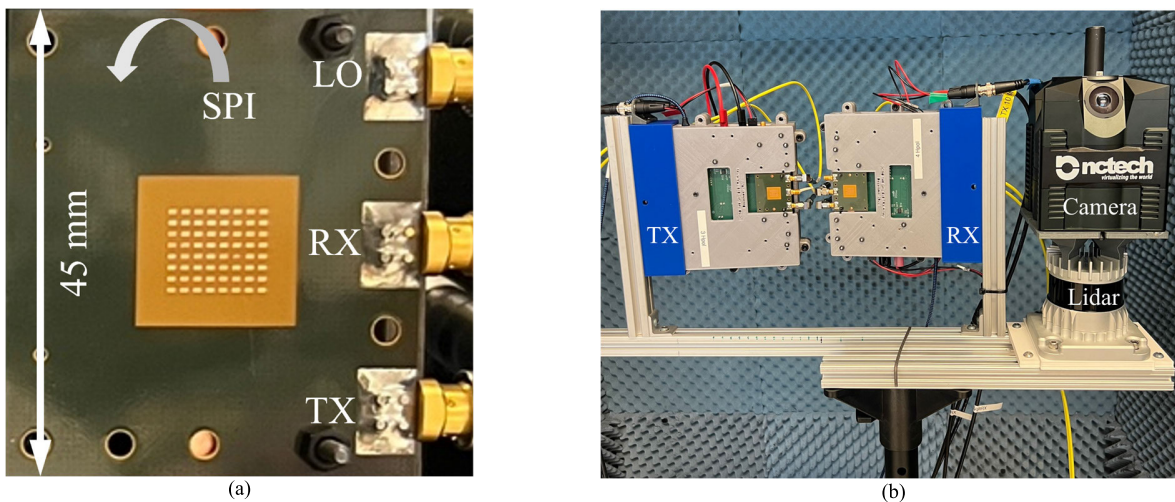


Fig. 1. NIST 141 GHz context-aware channel sounder. (a) Vertically polarized  $8 \times 8$  phased-array antenna board with separate TX, RX, and LO ports (the SPI port is on the back of the board). (b) TX and RX boards mounted in a monostatic configuration together with the camera and Lidar.

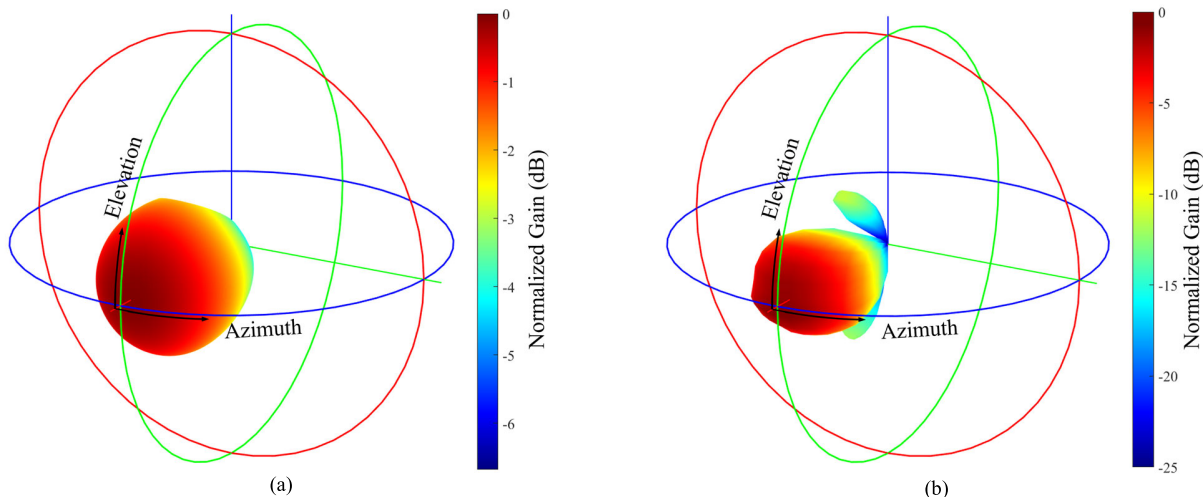


Fig. 2. Normalized 3-D antenna patterns of (a) single MSA with 3.5 dBi gain and (b) flat-top beam at TX with 25.1 dBi gain.

antennas and the TX and RX sections—and then we describe the camera/Lidar system, which provides context awareness of the target being sounded.

#### A. Phased-Array Antennas

Fig. 1(a) displays the 141 GHz  $8 \times 8$  phased-array antenna boards [57], [58] integrated into our channel sounder. The arrays are vertically polarized and can operate in either TX or RX mode. The 64 microstrip antennas (MSAs) are spaced roughly at half-wavelength: 1.2 mm in azimuth (horizontal) and 1.1 mm in elevation (vertical). The arrays can synthesize a beam within a FoV that corresponds to the half-power beamwidth of the individual antennas, which is  $\pm 39^\circ$  in azimuth and  $\pm 43^\circ$  in elevation. Fig. 2(a) shows the normalized radiation pattern of a single antenna, which has a 3.5 dBi boresight gain. An electronic beam is synthesized through analog beamforming, that is, by applying analog weights to the individual antennas to coherently phase their patterns. The weights are applied by independently programming the magnitude state (amplifier) and phase state (vector modulator)

of each antenna, which together form a complex amplitude, through a serial peripheral interface (SPI) port. The magnitude and phase state both have 4-bit precision, thus  $2^4 = 16$  possible values each. The SPI also features a channel select register to toggle each antenna on/off via its amplifier, so that the antennas can be calibrated individually. The arrays have onboard mixers for up- and down-converting the IF to RF through the local oscillator (LO) fed to the LO port, which multiplies that LO provided by a factor of six:  $\text{IF} + 6 \times \text{LO} = \text{RF}$ . The TX, RX, and LO ports can be seen in Fig. 1(a), whereas the SPI port is on the back of the board.

#### B. TX Section

The TX section is displayed in Fig. 1(b) and its block diagram in Fig. 3(a). The TX array illuminates the target under investigation by synthesizing a flat-top beam across its FoV through analog beamforming. While in principle the analog weights could be computed analytically [59], [60], better results were attained through a genetic algorithm, which could be tailored to the array specifications. Namely,

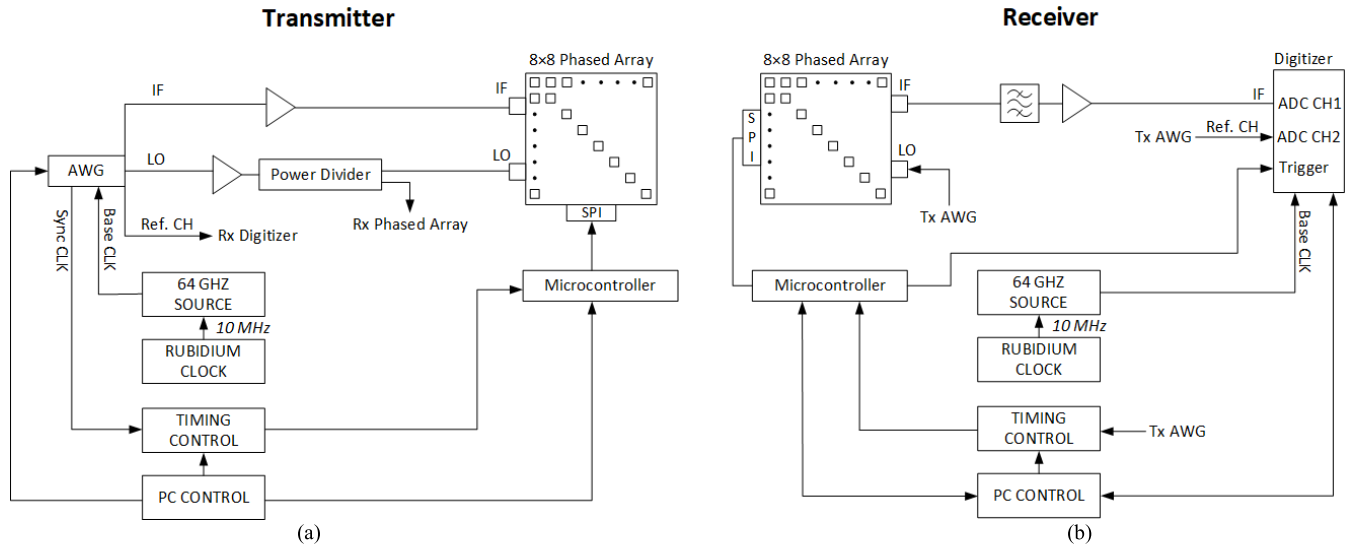


Fig. 3. Block diagram of the (a) TX section and (b) RX section.

it solved the integer programming problem of selecting the optimal analog weight for each antenna from the 256 possible values (16 magnitude states  $\times$  16 phase states). A genetic algorithm was chosen because it provides a good solution to the integer program with reasonable computation time. To solve the problem, the algorithm inputted the patterns of the individual antennas plus the 256 weight values. While we found the patterns to differ only slightly from antenna to antenna, we found the analog weights to differ significantly due to hardware nonidealities; as such, the 256 weight values were characterized per antenna using a VNA, namely as the  $S_{21}$  parameter at 141 GHz (see the setup in [53]). The objective of the integer program was to maximize the minimum beam gain over the array's FoV. Fig. 2(b) shows the corresponding normalized 3-D beam pattern we measured: the flat-top beam has  $32^\circ$  beamwidth in azimuth and  $30^\circ$  in elevation, with a boresight gain of 25.1 dBi.

The TX waveform, synthesized by an arbitrary waveform generator (AWG), is a repeating binary phase shift keying (BPSK)-modulated M-ary PN code with 2047 chip length (33.1 dB processing gain) and 6.4 GHz chip rate (6.4 GHz half-power bandwidth and 12.8 GHz null-to-null bandwidth). The code, denoted as  $p(\tau)$  in the delay domain  $\tau$ , is generated at baseband and modulated at IF by the AWG. Next, the IF signal is fed via a 12.4 dB power amplifier (including cable losses) to the array port at 5.7 dBm TX power and then mixed with an LO sourced by the same AWG. Adding the 25.1 dBi flat-top beam gain, the waveform was transmitted at 30.8 dBm equivalent isotropic radiated power (EIRP).

### C. RX Section

The RX section is displayed in Fig. 1(b) and its block diagram in Fig. 3(b). It generates a Radar image of the target, that is, a distribution of the complex power backscattered from the target in the 3-D domain: in azimuth ( $A$ ) and elevation ( $E$ ) AoA, denoted compactly as  $\theta = [\theta^A, \theta^E]$ , and in delay  $\tau$ . For every code transmitted, the RX signal is downconverted back

to IF, fed to a low noise amplifier (LNA), and then sampled by the digitizer at 32 GHz and digitally downconverted back to baseband. We denote the baseband RX signal as  $y(\tau)$ . The signal is correlated (convolved) with the known PN code in postprocessing, yielding the (complex) response  $(y * p^H)(\tau)$ , where  $*$  denotes the convolution operator and  $H$  the complex conjugate. In reality, five concatenated codes are transmitted and averaged at the RX to reduce the noise by 7 dB. The same LO sourced from the AWG for the TX board was extended to the RX board through a power divider, disciplined through a Rubidium clock.

The 30.8 dBm EIRP together with the effective processing gain of 27 dB of the PN code with predistortion filtering (see Section III-A), 3.5 dBi single antenna gain at the RX, 18.1 dB coherence gain of the RX array, 4 dB LNA gain (including the RX noise figure and cable losses), and a  $-71.5$  dBm noise floor corresponding to the 32 GHz digitizer sample rate yields a maximum measurable path loss of 154.9 dB.

The azimuth and elevation domains of the Radar image are generated by sweeping a beam within the RX array's FoV. Phased arrays, including ours, are designed to sweep the beam through analog beamforming, but to sweep the beam, the analog weights must be reprogrammed per sweep angle: it takes each array  $1.6 \mu\text{s}$  to program each antenna, or equivalently  $1.6 \mu\text{s} \times 64 = 102.4 \mu\text{s}$  to program all 64 antennas per sweep angle. The highest resolution image that is achievable given the 4-bit phase precision and the antenna spacing of our arrays is  $7.3^\circ$  in azimuth and  $6.3^\circ$  in elevation, translating to  $11 \times 12 = 132$  angles within the array's FoV. The total sweep would require  $102.4 \mu\text{s} \times 132 = 13.5$  ms, much beyond the targeted channel sweep duration of less than a millisecond. Rather, the switched beamforming technique we developed in [47] implements antenna switching instead of beam sweeping, by exploiting the channel select register to switch each antenna on and off sequentially, requiring  $0.8 \mu\text{s}$  for each antenna (half the programming time, since only the magnitude state is switched on/off). It then requires

only  $0.8 \mu\text{s} \times 64 = 51.2 \mu\text{s}$  to switch the antennas, 264 times faster than sweeping the beams. Once the individual antenna responses are measured, the switched beams can be formed in postprocessing by applying (computer) digital weights to the antenna responses. Critically, the switched beams can be swept at any angular resolution without changing the sweep duration.

While reducing the sweep duration by orders of magnitude is a significant benefit of switched beamforming, the other significant benefit is the accuracy that comes from the effectively infinite precision of digital weights compared to the 4-bit magnitude and 4-bit phase precision of the analog weights. Such precision allows us to generate Radar images at any angle resolution in far-field beamforming and, in near-field beamforming at any angle and at any delay resolution. However, where infinite precision matters most is in the fine calibration of the digital weights to compensate for the hardware nonidealities coupled with fine window tapering for sidelobe suppression, which together enable us to synthesize ideal beam patterns. All these features are essential to realizing real-time near-field beamforming, as we shall see later.

#### D. Context Awareness

The RF system as a unit generates a Radar image of the target. While it has been demonstrated that Radar images alone can be used for training deep learning models for target classification [2], [6], [7], [8], [9], [10], [11], [12], [13], [14], [15], [16], [17], [18], [19], [20], [21], to obtain classification accuracy above 90% with generalizability to at least ten different classes, the number of required training exemplars can be in the tens of thousands, necessitating months or even years to collect across targets with varying dimensions, colors, in different backgrounds, and so on, which can be prohibitively expensive and time consuming. Rather, when complementing the Radar images with digital twins of the target collected in real-time and in the same 3-D domain as the images, that can be reduced to less than a hundred [22].

To generate such digital twins, we mounted an NCTech iSTAR Pulsar panoramic camera and Ouster OS0-128 Lidar<sup>1</sup> pair that are flush with the RX section, as shown in Fig. 1(b). Critically, the separate local coordinates of the RF, camera, and Lidar systems must be spatially calibrated to a single global coordinate system, and separate clocks of the three systems must be temporally synchronized to capture the target at the same exact time instant. Details of how this is achieved as well as details of other applications for context-aware channel sounding are described in [49] and [50].

### III. CARRIER MULTIPLEXING

This section outlines the carrier multiplexing technique we developed to extend the instantaneous bandwidth of the arrays

<sup>1</sup>Certain commercial equipment, instruments, or materials are identified in this article to specify the experimental procedure adequately. Such identification is not intended to imply recommendation or endorsement by the National Institute of Standards and Technology (NIST), nor is it intended to imply that the materials or equipment identified are necessarily the best available for the purpose.

across their full RF passband. The approach involves transmitting PN codes on adjacent RF bands—each linked to a separate carrier frequency and each predistorted to compensate for the hardware nonidealities of the proper band—and subsequently multiplexing the signals received. We begin by describing the predistortion design for switched beamforming that we developed previously for a single band [47], [48]. We then introduce the novelty of this work: extending the design across multiple bands. We demonstrate that this technique doubles the bandwidth of our current arrays, translating to a tenfold increase in bandwidth for our next edition of the arrays, which feature an RF passband five times wider. Finally, we address practical considerations when implementing the technique.

#### A. Predistortion Filtering in a Single Band

When the TX and RX sections directly connected, the setup is referred to as a back-to-back configuration. The system is considered ideal if the RX signal matches the TX waveform exactly—in our case,  $y(\tau) = p(\tau)$  when the ideal code  $p(\tau)$  is transmitted. As outlined in Section II-C, the response  $(y * p^H)(\tau)$  is then equal to  $(p * p^H)(\tau)$ , which corresponds to the ideal impulse response shown in Fig. 4(a). This ideal impulse response exhibits a 66.2 dB dynamic range (peak-to-sidelobe ratio), the power equivalent of the ideal code's 33.1 dB processing gain. Its dual representation, the ideal frequency response  $P(f) \cdot P^H(f)$ , is illustrated in Fig. 4(b). In reality, no system is truly ideal due to the hardware nonidealities of the TX/RX sections. These imperfections introduce spurious pulses in the impulse response, which could be misclassified as reflections in the channel being sounded, reducing the dynamic range to just 21 dB, as shown in Fig. 4(a) without predistortion filtering. By employing predistortion filtering—transmitting a predistorted version of the code that compensates for the nonidealities instead of the ideal code—the spurious pulses can be suppressed.

The predistortion filter for switched beamforming was designed in an over-the-air (OTA) configuration [47], [53], [61], which, like a back-to-back configuration, accounts for the nonidealities of the TX/RX sections. However, it also addresses the nonidealities of the TX/RX array boards, which distort the response but cannot be accessed via connectors as in the back-to-back setup. Our OTA configuration replicates the operation of the channel sounder in the field: the TX and RX arrays are mounted on their respective sections and placed in an anechoic chamber, separated by  $d = 1$  m, with their normals aligned and pointed toward each other. The ideal code is transmitted and the RX array, with only antenna  $i$  switched on, receives the signal. This received signal is denoted as  $y_{\text{OTA}}^i(\tau)$ , with its frequency-domain equivalent represented as  $Y_{\text{OTA}}^i(f)$ . Furthermore, if the OTA channel, which incorporates distortion introduced by the TX/RX sections and the array boards, is denoted as  $h_{\text{OTA}}^i(\tau)$ , then the RX signal can be expressed as the convolution of the OTA channel with the ideal code, as follows:

$$y_{\text{OTA}}^i(\tau) = (h_{\text{OTA}}^i * p)(\tau). \quad (1a)$$

Now if the predistorted code  $\hat{p}^i(\tau)$  below is transmitted instead of the ideal code, where  $\mathcal{F}^{-1}$  denotes the inverse Fourier

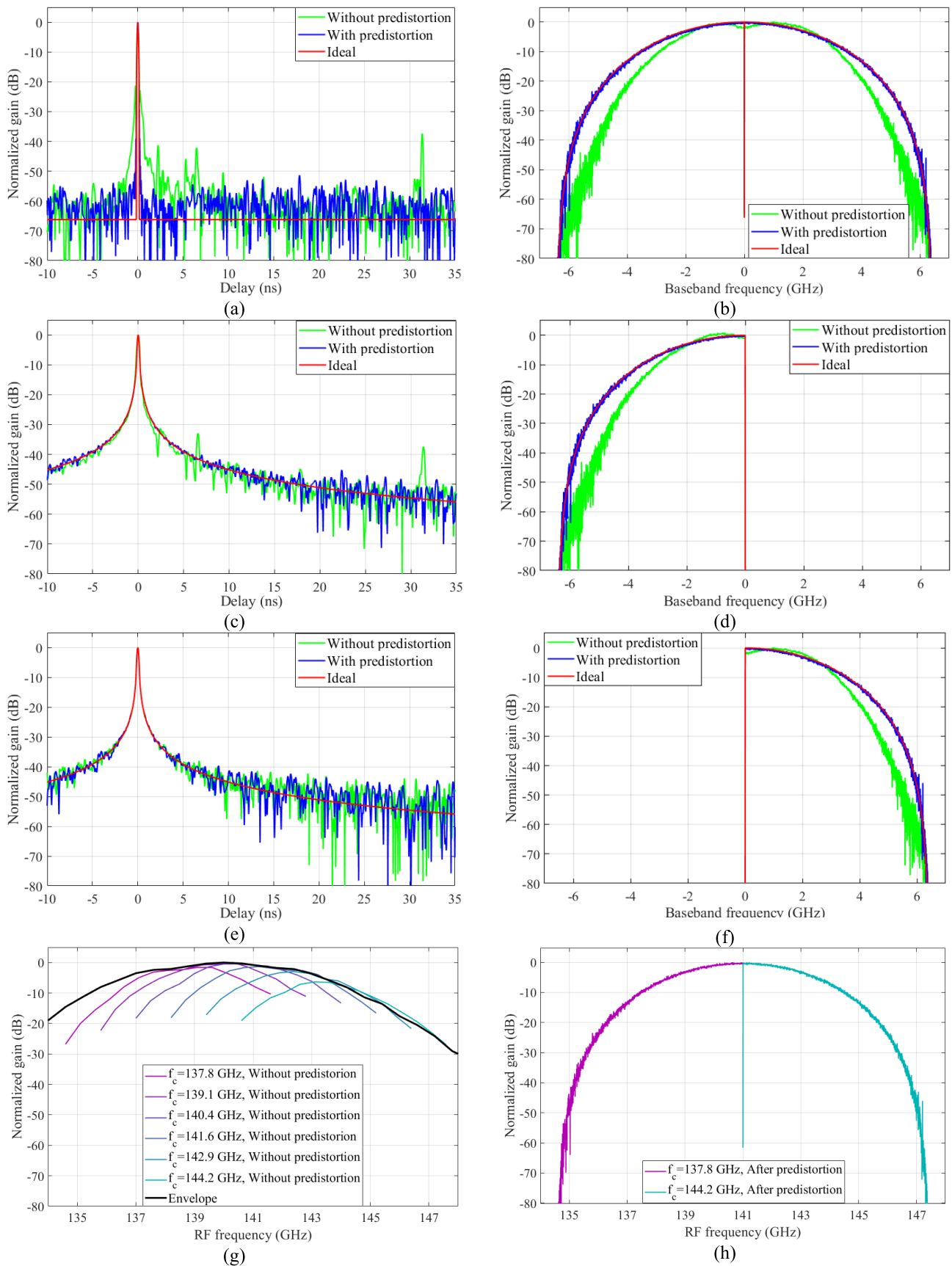


Fig. 4. Carrier multiplexing. (a) Delay and (b) frequency responses of the full 6.4 GHz baseband multiplexed across (c) delay and (d) frequency responses of the lower 3.2 GHz baseband and (e) delay and (f) frequency responses of the upper 3.2 GHz baseband. (g) Frequency response (before predistortion) of six bands with varying carrier frequency ( $f_c$ ) across the RF passband of the boards. (h) Frequency response (after predistortion) of the two bands used for carrier multiplexing.

transform

$$\hat{p}^i(\tau) = \left( \mathcal{F}^{-1} \left\{ \frac{P(f)}{Y_{\text{OTA}}^i(f)} \right\} * p \right)(\tau), \quad (1b)$$

then it is the ideal code that is recovered at the RX side:

$$\hat{y}_{\text{OTA}}^i(\tau) = (h_{\text{OTA}}^i * \hat{p}^i)(\tau) \approx p(\tau). \quad (1c)$$

In practice, the ideal code can only be recovered approximately, as predistortion cannot fully compensate for system nonlinearities. The detailed derivation of the predistorted code in (1b) is provided in [48].

In our original design [47], a unique predistorted code was transmitted per antenna switched on. We later observed that the other  $N - 1$  antennas cannot be entirely switched off in practice—there will always be leakage from the antenna that is switched on. To address this, an improved design [48] was developed in which the same predistorted code is transmitted across all antennas. This updated design is based on the RX signal that is received collectively from all antennas, inherently accounting for the mutual leakage between them. In the improved design [48], we transmit the same predistorted code across all antennas. However, the design is based on the RX signal received across all antennas, and so it inherently accounts for the mutual leakage between the antennas. First, the RX signals from all  $N$  antennas are summed:

$$y_{\text{OTA}}(\tau) = \frac{1}{N} \sum_{i=1}^N (h_{\text{OTA}}^i * p)(\tau). \quad (2a)$$

Then, the unique predistorted code  $\hat{p}(\tau)$  for all antennas is computed against the Fourier transform of the sum:

$$\hat{p}(\tau) = \left( \mathcal{F}^{-1} \left\{ \frac{P(f)}{Y_{\text{OTA}}(f)} \right\} * p \right)(\tau). \quad (2b)$$

Finally, the OTA response  $\hat{y}_{\text{OTA}}(\tau)$ , obtained by transmitting the predistorted code  $\hat{p}(\tau)$ , approximates the ideal code  $p(\tau)$ :

$$\hat{y}_{\text{OTA}}(\tau) = \frac{1}{N} \sum_{i=1}^N (h_{\text{OTA}}^i * \hat{p})(\tau) \approx p(\tau), \quad (2c)$$

as shown in Fig. 4(a). Transmitting the predistorted code in place of the ideal code extends the dynamic range from 21 dB to 54 dB, equivalent to 27 dB processing gain. Fig. 4(b) shows the OTA frequency response with and without predistortion filtering.

### B. Predistortion Filtering Over Multiple Bands

It is reported in [57] that the frequency response of the arrays can vary significantly across their RF passband. In fact, Fig. 4(g) shows the OTA frequency response (without predistortion) of six bands in the proximity of 141 GHz, which we generated by stepping the LO across adjacent carrier frequencies and sweeping the IF band for each LO. The bands each have an IF bandwidth of about 3.2 GHz, which corresponds to 28% fractional bandwidth at IF = 11.4 GHz, a value that falls within the typical Q-point range of operation. Note that the rolloff shown as a black envelope in Fig. 4(g), traced by stepping the LO continuously and plotting the peak

value in the bands, is gentler than the rolloffs across each of the individual bands. This is because the 3.2 GHz bandwidth corresponds to a fractional beamwidth of just 2.3% at 141 GHz carrier frequency once the bands are upconverted to RF.

The key realization in the carrier multiplexing technique proposed is that by exploiting the lower fractional bandwidth of the bands at RF, the instantaneous bandwidth can be extended by multiplexing the bands together. The technique is realized by transmitting codes on adjacent bands, by stepping the LO across adjacent carrier frequencies in rapid succession, and then summing the RX signals. The rapid stepping is achieved by sourcing the LO directly from the AWG (rather than from a voltage-controlled oscillator, as we did in the past)—it takes less than 5 ns to switch the LO. A further advantage is that the LO is phase locked to the IF signal produced by the AWG, so any AWG clock jitter will be mutual and thus will essentially cancel itself out. The disadvantage is that an additional AWG channel is required.

The codes for each band are individually predistorted to ensure that the summed OTA RX signals correspond to a single ideal code spanning the entire RF passband. For our current arrays, we consider two adjacent, nonoverlapping 3.2 GHz bands that together form the full 6.4 GHz band shown in Fig. 4(b). First, the ideal frequency response of the full band,  $P(f)$ , is partitioned into lower and upper bands, denoted as  $P^-(f)$  and  $P^+(f)$ , respectively. Distinct predistorted codes,  $\hat{p}^-(\tau)$  and  $\hat{p}^+(\tau)$ , are then computed for the respective OTA frequency responses,  $Y_{\text{OTA}}^-(f)$  and  $Y_{\text{OTA}}^+(f)$ , as follows:

$$y_{\text{OTA}}^-(\tau) = \frac{1}{N} \sum_{i=1}^N (h_{\text{OTA}}^{-,i} * p^-)(\tau) \quad (3a)$$

$$y_{\text{OTA}}^+(\tau) = \frac{1}{N} \sum_{i=1}^N (h_{\text{OTA}}^{+,i} * p^+)(\tau) \quad (3b)$$

$$\hat{p}^-(\tau) = \left( \mathcal{F}^{-1} \left\{ \frac{P^-(f)}{Y_{\text{OTA}}^-(f)} \right\} * p^- \right)(\tau) \quad (3c)$$

$$\hat{p}^+(\tau) = \left( \mathcal{F}^{-1} \left\{ \frac{P^+(f)}{Y_{\text{OTA}}^+(f)} \right\} * p^+ \right)(\tau). \quad (3d)$$

Finally, the OTA response,  $\hat{y}_{\text{OTA}}(\tau)$ , is expressed as the sum of the predistorted codes for both bands:

$$\hat{y}_{\text{OTA}}(\tau) = \frac{1}{N} \sum_{i=1}^N (h_{\text{OTA}}^{-,i} * \hat{p}^-)(\tau) + (h_{\text{OTA}}^{+,i} * \hat{p}^+)(\tau) \approx p(\tau). \quad (3e)$$

The ideal frequency response, as well as the frequency responses with and without predistortion filtering, are shown in Fig. 4(d) for the lower band and Fig. 4(f) for the upper band.

### C. Practical Considerations

In practice, we generate the ideal codes  $p^-(\tau)$  and  $p^+(\tau)$  at baseband by partitioning the full 12.4 GHz null-to-null band into two adjacent 6.4 GHz null-to-null bands, centered at  $-3.2$  GHz and  $3.2$  GHz, respectively. The objective is to match the two adjacent bands to the full band across the entire

null-to-null bandwidth. This is achieved by producing ideal codes at a 6.4 GHz chip rate, corresponding to the null-to-null bandwidth (not the half-power bandwidth). Notably, the spectra of the bands do not correspond to true PN codes; instead, they represent the half spectrum of a PN code. Furthermore, their half-power bandwidth is only 3.2 GHz, effectively smearing the 6.4 GHz rate chips. This smearing effect is evident in the impulse responses of the bands shown in Fig. 4(c) and (e), where the peaks are significantly duller than the impulse response of the full band in Fig. 4(a). Nevertheless, after multiplexing the bands, the impulse response of the full band aligns with that of an actual PN code.

To ensure that the basebands are centered at  $-3.2$  GHz and  $3.2$  GHz [Fig. 4(b)] remain adjacent after upconversion to 141 GHz—resulting in carrier frequencies of 137.8 GHz and 144.2 GHz [Fig. 4(h)]—special attention was given to the IF and LO design. The condition  $\text{IF} + 6 \times \text{LO} = 141$  GHz (from Section II-A) was satisfied precisely for each band. This required setting  $\text{LO} = 21.3$  GHz and  $\text{IF} = 13.2$  GHz for the lower band, and  $\text{LO} = 21.9$  GHz and  $\text{IF} = 9.6$  GHz for the upper band. In addition, to send the two band streams of five concatenated codes at 6.4 GHz chip rate ( $2 \times 5 \times 2047/6.4$  GHz =  $3.2 \mu\text{s}$ ) in addition to the antenna switching time ( $0.8 \mu\text{s}$ ), the LO switching time ( $0.005 \mu\text{s}$ ), and necessary guard times in between to account for clock jitter ( $1 \mu\text{s}$  each), we allocate  $8 \mu\text{s}$  per antenna for a total sweep time of  $8 \mu\text{s} \times 64 = 512 \mu\text{s}$ . Finally, any phase offset between the band codes must be compensated to ensure coherence across the full band. We observed that this offset was random for our AWG but remained fixed once the AWG was power up. Consequently, the offset had to be recomputed after each power cycle.

#### IV. NEAR-FIELD SWITCHED BEAMFORMING

For sensing applications, the near field is bound by the largest dimension among the target, the TX antenna aperture, and the RX antenna aperture. In this article, the focus application is finger recognition, and apropos, the width of the target—the human finger—ranges from 1.6 cm to 2 cm, which is slightly larger than the aperture lengths of the antenna arrays (1.3 cm). If defined by the Rayleigh distance ( $2D^2/\lambda$ ), where  $D = 2$  cm and  $\lambda = 0.21$  cm at 141 GHz carrier frequency, then the near field is bound by 38 cm. For our application, the target will typically be 10 cm to 20 cm from the sensor (the arrays in our case) [18], [19], so operation is indeed in the near field.

In this section, we describe how we realize near-field switched beamforming. First, we describe how we calibrate the digital beamforming weights, then we discuss the sensitivity of the weights to calibration.

##### A. Calibrated Digital Weights

As in analog beamforming, switched beamforming is implemented by applying complex weights to the array antennas—specifically to the antenna responses in postprocessing—to synthesize beams. Unlike far-field beamforming, where antenna weights are solely angle-dependent [62], near-field beamforming requires weights that are both angle- and

delay-dependent to accurately focus beams at close range. In addition, the curvature of spherical wavefronts in the near field introduces further complexity, demanding precise weight calculations beyond the capabilities of the onboard analog weights of the arrays. These challenges necessitate the use of switched beamforming, which provides the required precision by leveraging postprocessing techniques to achieve high-resolution near-field imaging and measurement.

The ideal near-field beamforming weight for antenna  $i$ , to steer the beam toward angle  $\theta$  and delay  $\tau$ , is [63]:

$$s^i(\theta, \tau) = w^i \cdot e^{j \frac{2\pi}{\lambda} \|c\tau(\cos\theta^A \cos\theta^E, \sin\theta^A \cos\theta^E, \sin\theta^E) - X^i\|_2}, \quad (4)$$

where  $X^i = (x^i, y^i, z^i)$  is the 3-D position of  $i^{\text{th}}$  antenna on the array and  $c$  is the speed of light. The Kaiser taper window  $w$  [64] was applied in (4) to suppress the beam sidelobes at the expense of widening the main lobe. The Kaiser window was chosen because it has a single tunable parameter  $\beta$  to balance the two factors. A value of  $\beta = 2.4$  was found empirically to achieve a favorable balance, enhancing suppression of the first lobe from 12.8 dB to 26.0 dB, while widening the azimuth beamwidth from  $13.0^\circ$  to  $16.3^\circ$  and the elevation beamwidth from  $11.4^\circ$  to  $14.4^\circ$ .

Section III-A describes a predistortion filter design for switched beamforming that reduces mutual leakage between the array antennas [48]. As part of the design to reduce leakage, the phase state of the analog weights is set randomly while to optimize the link budget their magnitude state is set to its maximum value. In light of these preset analog weights, the digital weights applied to the antenna responses will not be the ideal weights in (4); rather, to realize these ideal weights, they must be calibrated against the preset analog weights. Furthermore, to realize the ideal weights, the effect of predistortion filtering on the antenna responses must also be calibrated into the digital weights. To account for both factors in a single step, the OTA configuration in Section III-A was employed since both factors are embedded in the OTA response  $\hat{y}_{\text{OTA}}^i(\tau)$ . However, whereas in the past the digital weight calibration was—as the predistortion filter still is—applied only at a fixed angle [boresight,  $\theta = (0^\circ, 0^\circ)$ ] and for fixed distance  $d = 1$  m [47], [48], in this work the procedure was enhanced to account for the dependence of calibration on angle and—in relation to near-field beamforming—on distance (or the delay equivalent).

To account for angle dependence, the RX array was mounted on a 3-D rotator: for fixed distance  $d$ , the array was mechanically rotated to  $-\theta$  on a  $1^\circ$  grid within the array FoV and then electronically steered back into alignment with the TX boresight by applying the ideal digital weights  $s^i(\theta, \tau = d/c)$ . To account for delay dependence, the procedure above was repeated on a distance grid. Then, for each combined (angle, distance) grid point  $(\theta^j, \tau^j = d^j/c)$  indexed through  $j$ , the OTA response  $\hat{y}_{\text{OTA}}^{ij}(\tau)$  was recorded. Finally, the calibrated digital weights  $\hat{s}^i(\theta, \tau)$  were computed as follows:

$$\hat{s}^i(\theta, \tau) = s^i(\theta, \tau) \cdot \frac{s^i(\theta^j, \tau^j)}{\left(\hat{y}_{\text{OTA}}^{ij} * p^H\right)(\tau^j)}. \quad (5)$$

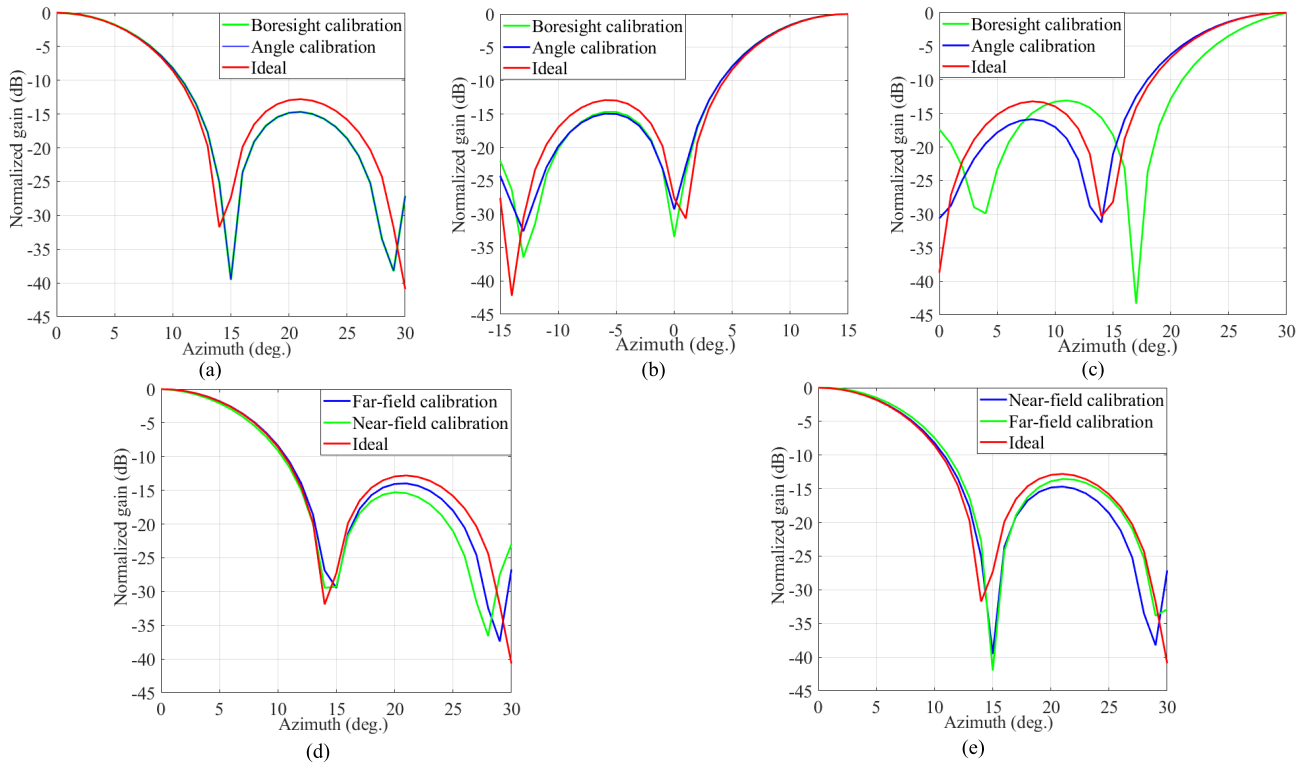


Fig. 5. Sensitivity of digital weights to calibration. Comparison of calibration at boresight only versus angle calibration when (a) scanning at  $\theta = (0^\circ, 0^\circ)$ , (b) scanning at  $\theta = (15^\circ, 15^\circ)$ , and (c) scanning at  $\theta = (30^\circ, 30^\circ)$ . Comparison of (d) calibration in the far-field on near-field data and (e) calibration in the near field on far-field data.

To implement the computation in (5), the grid point  $(\theta^j, \tau^j)$  closest to  $(\theta, \tau)$  was first identified. Then, the ideal weight  $s^i(\theta, \tau)$  was calibrated by the ratio between the ideal weight  $s^i(\theta^j, \tau^j)$  at the grid point and the recorded weight  $(\hat{y}_{\text{OTA}}^i * p^H)(\tau^j)$  at the correlation peak (at  $\tau^j$ ) of the OTA response. It follows that when the calibrated antenna response  $\hat{y}^i(\tau)$  is beamformed through the calibrated weights  $\hat{s}^i(\theta, \tau)$  to generate the 3-D Radar image:

$$u(\theta, \tau) = \frac{1}{N} \sum_{i=1}^N \hat{s}^i(\theta, \tau) \cdot \hat{y}^i(\tau), \quad (6)$$

it is analogous to beamforming the ideal antenna responses through the ideal weights.

Fig. 5(a)–(c) shows the calibrated antenna patterns versus the ideal antenna patterns of the boresight beam  $\theta = (0^\circ, 0^\circ)$ , together with two other illustrative beams at  $\theta = (15^\circ, 15^\circ)$  and  $\theta = (30^\circ, 30^\circ)$ , for the near-field distance  $d = 15$  cm. Thanks to switched beamforming, the calibrated patterns follow the ideal patterns very closely, in particular in the main lobe, with a maximum of 2.7 dB deviation from the ideal across the sidelobes of all three beams.

### B. Calibration Sensitivity

Although Fig. 5(a)–(c) demonstrates that quasi-ideal beams can be synthesized through switched beamforming with calibrated digital weights, calibration on such a dense angle grid (every  $1^\circ$  within the array FoV) translates to 6873 grid points, requiring about 90 h per distance. While the calibration is fully automated through programmed mechanical rotation, the amount of timing required is still formidable. As such, in this

section we investigate the sensitivity of the antenna pattern to calibration. Specifically, we investigate the sensitivity to angle and distance.

To highlight the dependence of calibration on an angle, in addition to the ideal patterns and angle-calibrated patterns, Fig. 5(a)–(c) also shows the patterns calibrated at boresight only, as we did in the past: While the boresight calibrated pattern of beam  $\theta = (15^\circ, 15^\circ)$  shows some degradation in the sidelobes compared to the angle calibrated pattern, degradation in the main lobe is minimal; however, degradation in both the sidelobes and in the main lobe of beam  $\theta = (30^\circ, 30^\circ)$  is significant. We conclude that angle calibration is beneficial, especially at the extreme angles within the array FoV.

To evaluate the dependence of calibration on distance, we compare calibration in the near field ( $d = 15$  cm) versus calibration in the far-field ( $d = 1$  m). Namely, Fig. 5(d) compares the two calibrations for the boresight beam pattern synthesized in the near field; the discrepancy between the two is minimal, especially in the main lobe. Fig. 5(e) also compares the two calibrations, however, for the boresight beam pattern synthesized in the far-field; again, the discrepancy between the two is minimal. We conclude that distance calibration is only marginally beneficial.

## V. CONTROLLED EXPERIMENTS

To validate the performance of the channel sounder, we conducted a series of controlled experiments with two metal cylinders having a 1.3 cm diameter, comparable to the width of a human finger. The advantage of metal cylinders over actual

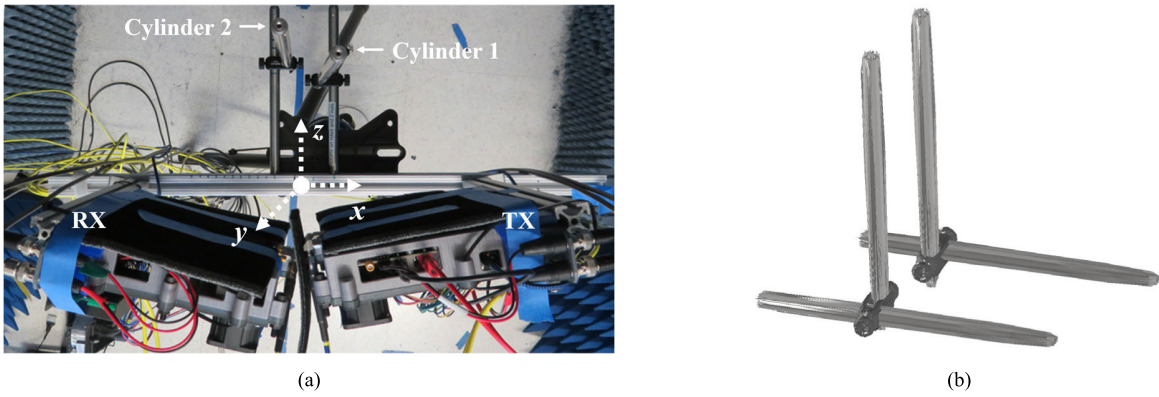


Fig. 6. Controlled experiments with two metal cylinders. (a) Bird's eye view of the monostatic setup. (b) Digital twin of target cylinders reconstructed from the camera and Lidar.

fingers is that they generate an ideal specular reflection whose angle and delay are known, hence serving as ground truth for comparison against estimated values. A bird's eye view of the monostatic setup is shown in Fig. 6(a). The absorber was attached to the front of the antenna units to minimize any scattering from the sounder hardware into the channel. Also displayed is the 3-D rectangular coordinate system  $\mathbf{X} = (x, y, z)$  and its origin, where the  $y$ -axis is perpendicular to the ground plane. In the controlled experiments, cylinder 1 was fixed at  $\mathbf{X} = [2.5, 0, 15]$  cm while cylinder 2 was displaced relatively; in Fig. 6(a), cylinder 2 is shown positioned at  $\mathbf{X} = [-1.5, 0, 16]$  cm. Fig. 6(b) shows a digital twin of the two target cylinders reconstructed from the camera and Lidar systems; the digital twin here takes the form of a 3-D mesh classified into three categories: cylinder 1, cylinder 2, and other. The 3-D image  $u(\mathbf{X})$  for each experiment was generated in rectangular coordinates by converting  $u(\theta, \tau)$  in (6) from spherical coordinates as follows:

$$\begin{aligned} u(\mathbf{X}) &= u(\theta, \tau) \\ x &= c\tau \cdot \sin\theta^A \cos\theta^E \\ y &= c\tau \cdot \sin\theta^A \sin\theta^E \\ z &= c\tau \cdot \cos\theta^E. \end{aligned} \quad (7)$$

In the first series of experiments, cylinder 2 was displaced from cylinder 1 along the  $x$  axis only. The associated sequence of images is displayed in Fig. 7(a)–(d). The two blobs in each image correspond to the individual cylinders and the peak power from cylinder 1's blob is marked with a white  $\mathbf{X}$ , for reference. The initial displacement between the cylinder centers was  $-3$  cm and was then incremented by  $-2$  cm,  $-4$  cm, and  $-6$  cm. For the initial displacement in Fig. 7(a), the system could not resolve the cylinders in the 2-D  $xy$  plane (upper plot) as they were spaced only 1.7 cm apart from edge-to-edge (considering their 1.3 cm diameter), and so appear as a single blob; however, through careful inspection in the full 3-D  $xyz$  domain, the single blob was indeed resolvable in the  $z$ -direction—the two blob centers are located at  $z = 13.7$  cm and at  $z = 15.5$  cm, hence 1.8 cm apart—thanks to the carrier multiplexed 6.4 GHz bandwidth that provides enhanced delay resolution. Nevertheless, after the first increment of  $-2$  cm in Fig. 7(b), the cylinders were already clearly resolvable in

the  $xy$  plane as well, and evermore after the increments of  $-4$  and  $-6$  cm in Fig. 7(c) and (d), respectively. As cylinder 2 was displaced along the  $x$ -axis, it actually moved farther and farther from the RX than cylinder 1, hence appears weaker and weaker. Some diffraction gratings between the edges of the cylinders are also noticeable.

In the second series of experiments shown in Fig. 7(e)–(h), cylinder 2 was again displaced from its initial position; however, this time along the  $z$ -axis by increments of  $+1$  cm. The initial separation of 1.7 cm along the  $z$ -axis in Fig. 7(e) widened notably after the first increment of 1 cm, as is apparent in the  $xyz$  domain in Fig. 7(f), with the separation increasing to 2 cm in Fig. 7(g) and then to 6 cm in Fig. 7(h), as expected. Notice that cylinder 1 starts to eclipse cylinder 2 evermore in Fig. 7(g) and (h), also as expected given their positioning with respect to the RX.

In the final series of experiments shown in Fig. 7(i) and (l), cylinder 2 was tilted from its initial position in increments of  $5^\circ$ , from tilted back at  $10^\circ$  to tilted forward at  $+5^\circ$ . The tilt changes the point of incidence on the cylinder, shifting cylinder 2's blob jointly along the  $+y$  and  $+z$ -axes with respect to cylinder 1's blob, exactly as observed in the images.

The RF estimation error, defined as the distance between the peak power in the 3-D image and the ground-truth location of the cylinder (measured on-site as its center in the  $x$ - $z$  plane), is compiled in Table I for the 12 experiments (a)–(l) per cylinder. Aside from experiments (a), (e), and (k), which actually correspond to the same initial position of cylinder 2 in the three series of displacements—for which the two cylinders are not clearly resolvable and so only well-defined peak is observed—the average estimation error across the other nine experiments and both cylinders is just 0.5 cm. The largest errors of these are for cylinder 2—1.5 cm and 2.5 cm in experiments (j) and (l), respectively—in the final series of displacements when the cylinder is tilted. In this series, the ground-truth location is the point of incidence of the specular reflection on the cylinder, calculated using geometrical optics from the TX and RX locations with the cylinder's location and tilt. Consequently, some of the RF estimation error most likely stems from uncertainties in the calculation.

Table I also includes the digital-twin estimation error, defined as the distance between the least-squares regression

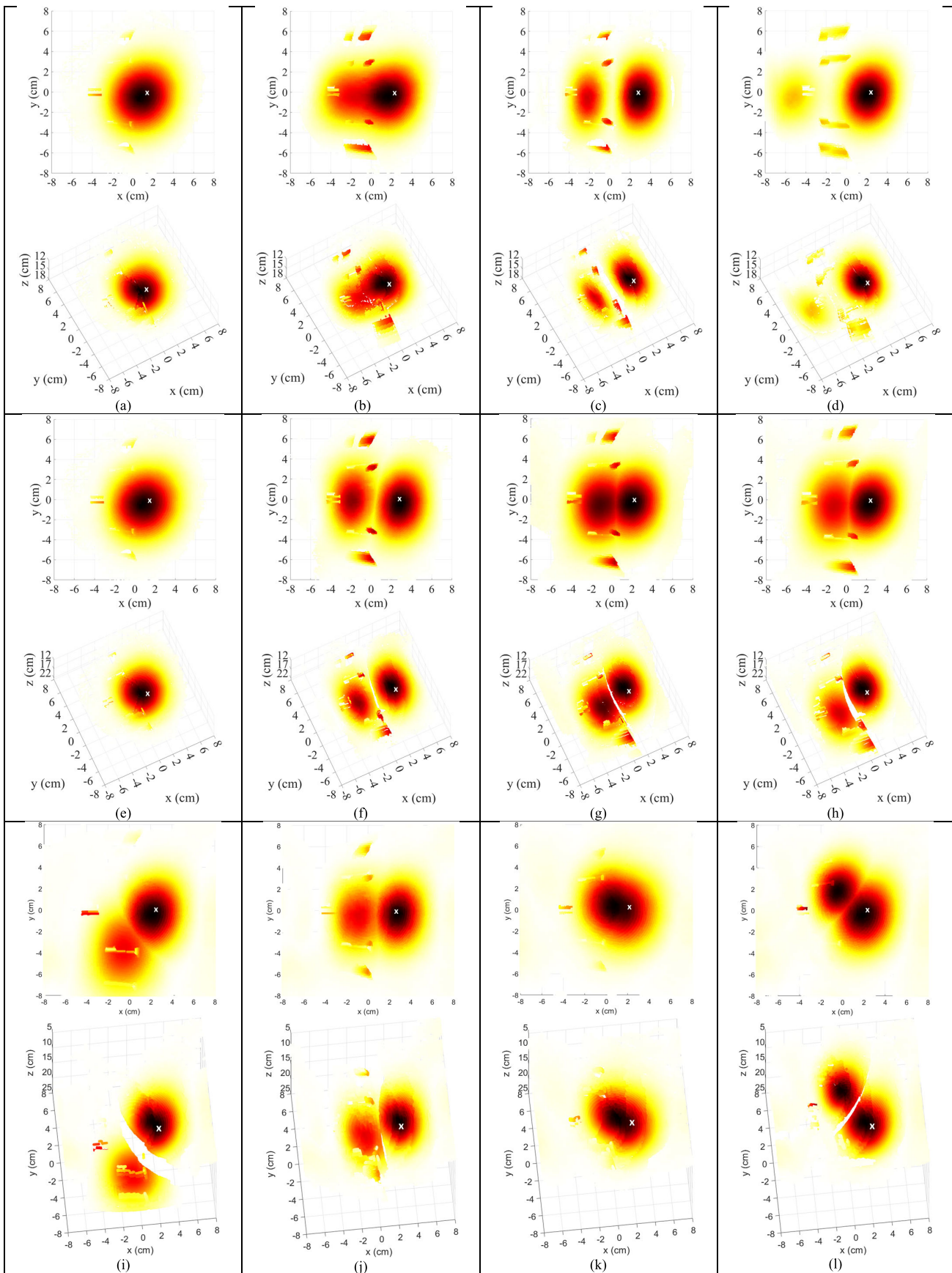


Fig. 7. Controlled experiments with two metal cylinders. (a)–(d) Series in which the cylinders are initially displaced by 3 cm along the  $x$ -axis only and then incrementally displaced by an additional  $-2$  cm, in the 2-D  $xy$  plane (upper plot) and in full 3-D  $xyz$  domain (lower plot) (e)–(h) Series in which the cylinders are initially displaced by 4 cm in the  $x$ -axis only and then incrementally displaced by an additional  $+1$  cm along the  $z$ -axis (i)–(l) Series in which the cylinders are initially displaced by 4 cm in the  $x$ -axis and 1 cm in the  $z$ -axis, and cylinder 2 is incrementally tilted by  $+5^\circ$  from  $-10^\circ$  to  $5^\circ$ .

TABLE I  
CYLINDER LOCATION ESTIMATION ERROR

Error (cm)	RF		Digital Twin	
	Cylinder 1	Cylinder 2	Cylinder 1	Cylinder 2
(a)	3.1	0.4	1.9	0.7
(b)	0.7	0.2	2.2	1.0
(c)	0.0	0.0	0.6	2.3
(d)	0.0	0.0	1.9	0.7
(e)	3.1	0.4	1.9	0.7
(f)	0.5	0.6	1.7	0.6
(g)	0.2	0.0	2.0	1.0
(h)	0.3	0.7	1.1	2.5
(i)	0.5	0.7	1.3	0.7
(j)	0.0	1.5	0.7	1.1
(k)	3.1	0.4	1.9	0.7
(l)	0.3	2.5	0.3	0.9

line fit to the cylinder's 3-D mesh and the cylinder's ground-truth location. The average error across the nine experiments and both cylinders is 1.3 cm, which is within the 2 cm tolerance provided in the Lidar manufacturer specifications. Finally, the Pearson correlation coefficient between the 24 RF estimation errors and the 24 digital-twin estimation errors was computed as 0.31, indicating that the errors from the two systems are uncorrelated.

## VI. CONCLUSION AND FUTURE WORK

We have implemented a 141 GHz channel sounder for JCAS applications. Thanks to electronic angle scanning by virtue of phased-array antennas and correlation-based sounding, a complete directional channel sweep can be completed in just 512  $\mu$ s, for real-time measurement. And thanks to switched beamforming instead of analog beamforming, near-field beamforming—whose weights are both delay and angle dependent and so requires phase precision beyond the 4 bits available on the array boards—is implemented through the effectively infinite precision of computer digital weights applied in postprocessing to the antenna responses switched on individually. Together with fine hardware calibration, controlled experiments on metal cylinders demonstrate 3-D imaging resolution on the order of 2 cm, all while complementing the RF images with spatially and temporally synchronized camera images and Lidar point clouds to generate real-time digital twins for AI-assisted channel modeling.

Of note, the carrier multiplexing technique proposed that doubles the 3.2 GHz IF bandwidth of the boards to saturate the 6.4 GHz RF bandwidth will be particularly applicable to the next edition of 141 GHz phased-array boards currently under development, slated for 32 GHz RF bandwidth. For these, we will be able to exploit a total of ten bands across 32 GHz<sup>2</sup> instead of just two across 6.4 GHz, increasing the delay resolution by a factor of five. The boards will also feature 16  $\times$  16 dual-polarized antennas. Aside from dual polarization, the

<sup>2</sup>Although it is pointed out in [65] that bandwidths at 141 GHz are not expected to exceed 7.5 GHz, in channel sounding it is beneficial to implement the widest bandwidth obtainable, for maximum application flexibility—the resultant channel can always be downsampled to lower bandwidths but the converse is not possible.

angle resolution in azimuth and elevation will be doubled and power quadrupled by virtue of the larger dimensions.

## REFERENCES

- [1] J. Wang, N. Varshney, C. Gentile, S. Blandino, J. Chuang, and N. Golmie, "Integrated sensing and communication: Enabling techniques, applications, tools and data sets, standardization, and future directions," *IEEE Internet Things J.*, vol. 9, no. 23, pp. 23416–23440, Dec. 2022.
- [2] M. Zhao et al., "Through-wall human pose estimation using radio signals," in *Proc. IEEE/CVF Conf. Comput. Vis. Pattern Recognit.*, Salt Lake City, UT, USA, Jun. 2018, pp. 7356–7365.
- [3] S. Gupta, P. K. Rai, A. Kumar, P. K. Yalavarthi, and L. R. Cenkaramaddi, "Target classification by mmWave FMCW radars using machine learning on range-angle images," *IEEE Sensors J.*, vol. 21, no. 18, pp. 19993–20001, Sep. 2021.
- [4] A. Sengupta, F. Jin, R. Zhang, and S. Cao, "mm-Pose: Real-time human skeletal posture estimation using mmWave radars and CNNs," *IEEE Sensors J.*, vol. 20, no. 17, pp. 10032–10044, Sep. 2020.
- [5] H. Xue et al., "MmMesh: Towards 3D real-time dynamic human mesh construction using millimeter-wave," in *Proc. 19th Annu. Int. Conf. Mobile Syst., Appl., Services*, New York City, NY, USA, Jun. 2021, pp. 269–282.
- [6] A. D. Singh, S. S. Sandha, L. Garcia, and M. Srivastava, "RadHAR: Human activity recognition from point clouds generated through a millimeter-wave radar," in *Proc. 3rd ACM Workshop Millimeter-Wave Netw. Sens. Syst.*, Los Cabos, Mexico, Oct. 2019, pp. 51–56.
- [7] R. Zhang and S. Cao, "Real-time human motion behavior detection via CNN using mmWave radar," *IEEE Sensors Lett.*, vol. 3, no. 2, pp. 1–4, Feb. 2019.
- [8] A. Pesin, A. Louzir, and A. Haskou, "A novel approach for radar-based human activity detection and classification," in *Proc. IEEE Int. Conf. Consum. Electron. (ICCE)*, Las Vegas, NV, USA, Jan. 2021, pp. 1–4.
- [9] Y. Zhao, V. Sark, M. Krstic, and E. Grass, "Novel approach for gesture recognition using mmWave FMCW RADAR," in *Proc. IEEE 95th Veh. Technol. Conf.*, Helsinki, Finland, Jun. 2022, pp. 1–6.
- [10] Y. Zhao, V. Sark, M. Krstic, and E. Grass, "Low complexity radar gesture recognition using synthetic training data," *Sensors*, vol. 23, no. 1, p. 308, Dec. 2022.
- [11] Y. Zhao, V. Sark, M. Krstic, and E. Grass, "Synthetic training data generator for hand gesture recognition based on FMCW RADAR," in *Proc. 23rd Int. Radar Symp. (IRS)*, Gdańsk, Poland, Sep. 2022, pp. 463–468.
- [12] H. Liu et al., "M-gesture: Person-independent real-time in-air gesture recognition using commodity millimeter wave radar," *IEEE Internet Things J.*, vol. 9, no. 5, pp. 3397–3415, Mar. 2022.
- [13] Y. Li et al., "Towards domain-independent and real-time gesture recognition using mmWave signal," *IEEE Trans. Mobile Comput.*, vol. 22, no. 12, pp. 7355–7369, Dec. 2023.
- [14] J.-T. Yu, L. Yen, and P.-H. Tseng, "mmWave radar-based hand gesture recognition using range-angle image," in *Proc. IEEE 91st Veh. Technol. Conf. (VTC-Spring)*, Antwerp, Belgium, May 2020, pp. 1–5.
- [15] A. Ninos, J. Hasch, and T. Zwick, "Real-time macro gesture recognition using efficient empirical feature extraction with millimeter-wave technology," *IEEE Sensors J.*, vol. 21, no. 13, pp. 15161–15170, Jul. 2021.
- [16] A. Ninos, J. Hasch, and T. Zwick, "Multi-user macro gesture recognition using mmWave technology," in *Proc. 18th Eur. Radar Conf. (EuRAD)*, London, U.K., Apr. 2022, pp. 37–40.
- [17] A. Ali et al., "End-to-end dynamic gesture recognition using mmWave radar," *IEEE Access*, vol. 10, pp. 88692–88706, 2022.
- [18] X. Ma, Y. Zhao, L. Zhang, Q. Gao, M. Pan, and J. Wang, "Practical device-free gesture recognition using WiFi signals based on metalearning," *IEEE Trans. Ind. Informat.*, vol. 16, no. 1, pp. 228–237, Jan. 2020.
- [19] Y. Kim and B. Toomajian, "Hand gesture recognition using micro-Doppler signatures with convolutional neural network," *IEEE Access*, vol. 4, pp. 7125–7130, 2016.
- [20] Z. Zhang, Z. Tian, and M. Zhou, "Latern: Dynamic continuous hand gesture recognition using FMCW radar sensor," *IEEE Sensors J.*, vol. 18, no. 8, pp. 3278–3289, Apr. 2018.
- [21] Y. Ren et al., "Hand gesture recognition using 802.11ad mmWave sensor in the mobile device," in *Proc. IEEE Wireless Commun. Netw. Conf. Workshops (WCNCW)*, Nanjing, China, Mar. 2021, pp. 1–6.
- [22] R. Caromi et al., "Human gesture classification through keypoint-integrated deep learning on millimeter-wave radar," *IEEE Trans. Hum.-Mach. Syst.*, Submitted to.

- [23] Y. Xing and T. S. Rappaport, "Propagation measurement system and approach at 140 GHz-moving to 6G and above 100 GHz," in *Proc. IEEE Global Commun. Conf. (GLOBECOM)*, Abu Dhabi, UAE, Dec. 2018, pp. 1–6.
- [24] Y. Lyu, P. Kyösti, and W. Fan, "Sub-terahertz channel sounder: Review and future challenges," *China Commun.*, vol. 20, no. 6, pp. 26–48, Jun. 2023.
- [25] A. Ghosh and M. Kim, "THz channel sounding and modeling techniques: An overview," *IEEE Access*, vol. 11, pp. 17823–17856, 2023.
- [26] C.-L. Cheng, S. Kim, and A. Zajic, "Comparison of path loss models for indoor 30 GHz, 140 GHz, and 300 GHz channels," in *Proc. 11th Eur. Conf. Antennas Propag. (EuCAP)*, Paris, France, Mar. 2017, pp. 716–720.
- [27] K. Du, O. Ozdemir, F. Erden, and I. Guvenc, "Sub-terahertz and mmWave penetration loss measurements for indoor environments," in *Proc. IEEE Int. Conf. Commun. Workshops*, Montreal, QC, Canada, Jun. 2021, pp. 1–6.
- [28] B. De Beelde, E. Tanghe, D. Plets, and W. Joseph, "Indoor radio channel modeling at D-band frequencies," in *Proc. 16th Eur. Conf. Antennas Propag. (EuCAP)*, Madrid, Spain, Mar. 2022, pp. 1–4.
- [29] N. A. Abbasi, A. F. Molisch, and J. C. Zhang, "Measurement of directionally resolved radar cross section of human body for 140 and 220 GHz bands," in *Proc. IEEE Wireless Commun. Netw. Conf. Workshops (WCNCW)*, Seoul, (South) Korea, Apr. 2020, pp. 1–4.
- [30] S. L. H. Nguyen, K. Haneda, and J. Putkonen, "Dual-band multipath cluster analysis of small-cell backhaul channels in an urban street environment," in *Proc. IEEE Globecom Workshops*, Washington, DC, USA, Dec. 2016, pp. 1–6.
- [31] S. L. H. Nguyen, K. Haneda, J. Järveläinen, A. Karttunen, and J. Putkonen, "Large-scale parameters of spatio-temporal short-range indoor backhaul channels at 140 GHz," in *Proc. IEEE 93rd Veh. Technol. Conf. (VTC-Spring)*, Helsinki, Finland, Apr. 2021, pp. 1–6.
- [32] B. De Beelde, E. Tanghe, D. Plets, and W. Joseph, "Outdoor line-of-sight path loss modeling at 140 GHz," in *Proc. 16th Eur. Conf. Antennas Propag. (EuCAP)*, Madrid, Spain, Mar. 2022, pp. 1–4.
- [33] G. Song et al., "Channel measurement and characterization at 140 GHz in a wireless data center," in *Proc. IEEE Global Commun. Conf.*, Rio de Janeiro, Brazil, Dec. 2022, pp. 4764–4769.
- [34] Y. Lyu, P. Kyösti, and W. Fan, "Sub-THz VNA-based channel sounder structure and channel measurements at 100 and 300 GHz," in *Proc. IEEE 32nd Annu. Int. Symp. Pers., Indoor Mobile Radio Commun. (PIMRC)*, Helsinki, Finland, Sep. 2021, pp. 1–5.
- [35] N. A. Abbasi et al., "Double-directional channel measurements for urban THz communications on a linear route," in *Proc. IEEE Int. Conf. Commun. Workshops (ICC Workshops)*, Montreal, QC, Canada, Jun. 2021, pp. 1–6.
- [36] N. A. Abbasi et al., "THz band channel measurements and statistical modeling for urban D2D environments," *IEEE Trans. Wireless Commun.*, vol. 22, no. 3, pp. 1466–1479, Mar. 2023.
- [37] Y. Lyu, Z. Yuan, F. Zhang, P. Kyösti, and W. Fan, "Virtual antenna array for W-band channel sounding: Design, implementation, and experimental validation," *IEEE J. Sel. Topics Signal Process.*, vol. 17, no. 4, pp. 729–744, Jul. 2023.
- [38] P. Kyösti, K. Haneda, J.-M. Conrat, and A. Pärssinen, "Above-100 GHz wave propagation studies in the European project Hexa-X for 6G channel modelling," in *Proc. Joint Eur. Conf. Netw. Commun. 6G Summit (EuCNC/6G Summit)*, Porto, Portugal, Jun. 2021, pp. 538–543.
- [39] P. Sen et al., "Terahertz communications can work in rain and snow: Impact of adverse weather conditions on channels at 140 GHz," in *Proc. 6th ACM Workshop Millimeter-Wave Terahertz Netw. Sens. Syst.*, Sydney, NSW, Australia, Oct. 2022, pp. 13–18.
- [40] R. Tanski et al., "Sub-THz wireless channel field measurements: A study at 140 GHz," in *Proc. IEEE Globecom Workshops (GC Wkshps)*, Rio de Janeiro, Brazil, Dec. 2022, pp. 1790–1795.
- [41] D. Bodet, P. Dinh, M. Stojanovic, J. Widmer, D. Koutsonikolas, and J. M. Jornet, "Characterizing sub-THz MIMO channels in practice: A novel channel sounder with absolute time reference," in *Proc. IEEE Global Commun. Conf.*, Kuala Lumpur, Malaysia, Dec. 2023, pp. 1459–1464.
- [42] S. Ju and T. S. Rappaport, "140 GHz urban microcell propagation measurements for spatial consistency modeling," in *Proc. IEEE Int. Conf. Commun.*, Montreal, QC, Canada, Jun. 2021, pp. 1–6.
- [43] S. Ju, Y. Xing, O. Kanhere, and T. S. Rappaport, "Millimeter wave and sub-terahertz spatial statistical channel model for an indoor office building," *IEEE J. Sel. Areas Commun.*, vol. 39, no. 6, pp. 1561–1575, Jun. 2021.
- [44] H. Tataria, M. Shafi, A. F. Molisch, M. Dohler, H. Sjöland, and F. Tufvesson, "6G wireless systems: Vision, requirements, challenges, insights, and opportunities," *Proc. IEEE*, vol. 109, no. 7, pp. 1166–1199, Jul. 2021.
- [45] Q. Zhu, C. Wang, B. Hua, K. Mao, S. Jiang, and M. Yao, "3GPP TR 38.901 channel model," in *The Wiley 5G Ref: The Essential 5G Reference Online*. Hoboken, NJ, USA: Wiley Press, 2021, pp. 1–35.
- [46] T. S. Rappaport, *Wireless Communications: Principles and Practice*. Cambridge, U.K.: Cambridge Univ. Press, 2024.
- [47] D. Caudill, J. Chuang, S. Y. Jun, C. Gentile, and N. Golmie, "Real-time mmWave channel sounding through switched beamforming with 3-D dual-polarized phased-array antennas," *IEEE Trans. Microw. Theory Techn.*, vol. 69, no. 11, pp. 5021–5032, Nov. 2021.
- [48] D. Caudill, J. Chuang, C. Gentile, and S. Y. Jun, "On predistortion filtering for switched beamforming with phased-array antennas," in *Proc. 17th Eur. Conf. Antennas Propag. (EuCAP)*, Florence, Italy, Mar. 2023, pp. 1–5.
- [49] A. Bodi, S. Berweger, R. Caromi, J. Bang, J. Senic, and C. Gentile, "AI-based environment segmentation using a context-aware channel sounder," in *Proc. 18th Eur. Conf. Antennas Propag. (EuCAP)*, Glasgow, U.K., Mar. 2024, pp. 1–5.
- [50] J. Chuang et al., "Quasi-deterministic channel propagation model for human sensing: Gesture recognition use case," *IEEE Open J. Antennas Propag.*, vol. 5, pp. 557–572, 2024.
- [51] P. B. Papazian, C. Gentile, K. A. Remley, J. Senic, and N. Golmie, "A radio channel sounder for mobile millimeter-wave communications: System implementation and measurement assessment," *IEEE Trans. Microw. Theory Techn.*, vol. 64, no. 9, pp. 2924–2932, Sep. 2016.
- [52] R. Sun et al., "Design and calibration of a double-directional 60 GHz channel sounder for multipath component tracking," in *Proc. 11th Eur. Conf. Antennas Propag. (EuCAP)*, Davos, Switzerland, Mar. 2017, pp. 3336–3340.
- [53] D. Caudill, P. B. Papazian, C. Gentile, J. Chuang, and N. Golmie, "Omnidirectional channel sounder with phased-array antennas for 5G mobile communications," *IEEE Trans. Microw. Theory Techn.*, vol. 67, no. 7, pp. 2936–2945, Jul. 2019.
- [54] S. Blandino, J. Senic, C. Gentile, D. Caudill, J. Chuang, and A. Kayani, "Markov multi-beam tracking on 60 GHz mobile channel measurements," *IEEE Open J. Veh. Technol.*, vol. 3, pp. 26–39, 2022.
- [55] N. Varshney et al., "Adaptive channel-state-information feedback in integrated sensing and communication systems," *IEEE Internet Things J.*, vol. 10, no. 24, pp. 22469–22486, Dec. 2023.
- [56] J. Wang, J. Chuang, S. Berweger, C. Gentile, and N. Golmie, "Toward opportunistic radar sensing using millimeter-wave Wi-Fi," *IEEE Internet Things J.*, vol. 11, no. 1, pp. 188–200, Jan. 2024.
- [57] S. Li, Z. Zhang, B. Rupakula, and G. M. Rebeiz, "An eight-element 140-GHz wafer-scale IF beamforming phased-array receiver with 64-QAM operation in CMOS RFSOI," *IEEE J. Solid-State Circuits*, vol. 57, no. 2, pp. 385–399, Feb. 2022.
- [58] A. Ahmed, L. Li, M. Jung, S. Li, D. Baltimas, and G. M. Rebeiz, "140-GHz 2-D scalable on-grid  $8 \times 8$ -element transmit-receive phased arrays with up/down converters demonstrating a 5.2-m link at 16 Gbps," *IEEE Trans. Microw. Theory Techn.*, vol. 72, no. 5, pp. 2852–2868, May 2024.
- [59] H. J. Orchard, R. S. Elliott, and G. J. Stern, "Optimising the synthesis of shaped beam antenna patterns," *IEE Proc. H*, vol. 132, pp. 63–68, Feb. 1985.
- [60] K. Kibaroglu, M. Sayginer, T. Phelps, and G. M. Rebeiz, "A 64-element 28-GHz phased-array transceiver with 52-dBm EIRP and 8–12-Gb/s 5G link at 300 meters without any calibration," *IEEE Trans. Theory Techn.*, vol. 66, no. 12, pp. 5796–5811, Dec. 2018.
- [61] S. Y. Jun, D. Caudill, J. Senic, C. Gentile, J. Chuang, and N. Golmie, "Over-the-air calibration of a dual-beam dual-polarized 28-GHz phased-array channel sounder," in *Proc. IEEE Int. Symp. Antennas Propag. North Amer. Radio Sci. Meeting*, Montreal, QC, Canada, Jul. 2020, pp. 1093–1094.
- [62] D. K. Cheng, *Fundamentals of Engineering Electromagnetics*. Reading, MA, USA: Addison-Wesley, 1993.
- [63] M. Cui and L. Dai, "Near-field wideband beamforming for extremely large antenna arrays," *IEEE Trans. Wireless Commun.*, vol. 23, no. 10, pp. 13110–13124, Oct. 2024.
- [64] A. V. Oppenheim, *Discrete-Time Signal Processing*. London, U.K.: Pearson, 1999.
- [65] *Enhanced Measurement Campaigns and Analysis at D-Band Frequencies*, document THz002, v1.1.1, ETSI, Feb. 2023.



**Jihoon Bang** received the Ph.D. degree in electronic engineering from Hanyang University, Seoul, South Korea, in 2022.

From March 2022 to August 2022, he worked as a Post-Doctoral Fellow at the 5G and Unmanned Vehicle Research Center, Hanyang University. Since September 2022, he has been working as a Post-Doctoral Researcher at the Communications Technology Laboratory, National Institute of Standards and Technology (NIST), Boulder, CO, USA, where he is currently involved in the NextG Channel Measurement and Modeling Project and the development of phased-array channel sounders. His current research interests include sub-terahertz antennas and wireless systems for next-generation communications.



**Samuel Berweger** received the Ph.D. degree from the University of Washington, Seattle, WA, USA, in 2011.

He joined at the National Institute of Standards and Technology (NIST), Boulder, CO, USA, in 2013. In 2022 he joined the NIST Communications Technology Laboratory to pursue interests in channel sounding and advanced free-space RF propagation measurements. His past research interests include were focused on scanning probe-based sub-diffraction limit microscopy at optical and microwave frequencies.



**Jack Chuang** received the Ph.D. degree from The Pennsylvania State University, State College, PA, USA, in 2008.

He was a Graduate Research Assistant at the Communications and Space Sciences Laboratory, The Pennsylvania State University. He then worked with BAE Systems, Merrimack, NH, USA, in electronic warfare and Cisco Systems, Richfield, OH, USA, in spectrum sharing. He is currently with the Communication Technology Laboratory, NIST, Gaithersburg, MD, USA, developing 5G mmWave channel sounders.



**Camillo Gentile** (Member, IEEE) received the Ph.D. degree in electrical engineering from The Pennsylvania State University, University Park, PA, USA, in 2001.

He joined at the National Institute of Standards and Technology (NIST), Gaithersburg, MD, USA, in 2001, as a Research Engineer at the Information Technology Laboratory, and since 2014, he has been at the Communications Technology Laboratory. He initiated the Radio Access and Propagation Metrology Group in 2021 and led the group until 2023. He is currently leading the NextG Channel Measurement and Modeling Project. He has co-authored over 100 peer-reviewed journal and conference papers, and two books: *Geolocation Techniques* (Springer, 2012) and *Radio Propagation Measurements and Channel Modeling: Best Practices in Millimeter-Wave and Sub-Terahertz Frequencies* (Cambridge University Press, 2022). His recent research interests include channel modeling and physical-layer modeling for joint communications and sensing systems.



**Nada Golmie** (Fellow, IEEE) received the Ph.D. degree in computer science from the University of Maryland, College Park, MD, USA, in 2002.

Since 1993, she has been a Research Engineer with the National Institute of Standards and Technology (NIST), Gaithersburg, MD, USA. From 2014 to 2022, she was the Chief of Wireless Networks Division with NIST. She is currently a NIST Fellow with the Communications Technology Laboratory. She is the Author of *Coexistence in Wireless Networks: Challenges and System-level Solutions in the Unlicensed Bands*, published by Cambridge University Press in 2006. Her research interests include media access control and protocols for wireless networks led to more than 200 technical articles presented at professional conferences, journals, and contributed to international standard organizations and industry led consortia. She leads several Projects related to the modeling and evaluation of future generation wireless systems and protocols and the NextG Channel Model Alliance Chair.



**Sebastian Semper** received the Master of Science degree and the Ph.D. degree (Hons.) in electrical engineering from Technische Universitaet Ilmenau, Ilmenau, Germany, in 2015 and 2022, respectively. He studied mathematics at Technische Universität Ilmenau, (TU Ilmenau), Ilmenau, Germany.

Since 2015, he has been a Research Assistant from the Electronic Measurements and Signal Processing Group, which is a joint research activity between the Fraunhofer Institute for Integrated Circuits IIS and TU Ilmenau, Ilmenau. Since then, he has been a Post-Doctoral Student with the Electronic Measurements and Signal Processing Group. In 2023, he spent six months with the Wireless Networks Division, National Institute of Standards and Technology (NIST), Gaithersburg, MD, USA, where he worked on various channel sounding systems and related algorithms. His research interests consist of compressive sensing, parameter estimation, optimization, numerical methods and algorithm design.